Solid obstacles can reduce hydrodynamic loading during water entry

M. Jalalisendi, G. Benbelkacem, and M. Porfiri

Phys. Rev. Fluids **3**, 074801 — Published 20 July 2018
DOI: 10.1103/PhysRevFluids.3.074801

Solid obstacles can reduce hydrodynamic loading during water entry

M. Jalalisendi, G. Benbelkacem, and M. Porfiri*
Department of Mechanical and Aerospace Engineering,
New York University Tandon School of Engineering,
Brooklyn, NY 11201, USA

The notion of sympathetic interactions between solids immersed in fluids is ubiquitous in applied physics, and the complexity of these interactions often results in unexpected outcomes. In this paper, we study the water entry of a rigid wedge in the presence of a neutrally-buoyant solid cylinder below the water surface. We combine particle image velocimetry and direct measurements to elucidate the fluid-structure interaction. While the fluid confinement from the cylinder elicits a predictable increase in the pressure close to the keel, it is also responsible for a surprising reduction in the pressure toward the pile-up. Through a detailed solution based on potential flow theory, we offer an explanation for this phenomenon. Our results may find application in the study of marine vessels that maneuver in occluded waters and seabirds that plunge and dive close to rocks or ice.

PACS numbers: 46.40.Jj, 47.55.dr, 47.80.Fg, 47.80.Jk, 47.85.Dh

I. INTRODUCTION

Water entry refers to a general class of problems in which a solid body, rigid or compliant, "enters" the surface of an otherwise quiescent fluid at a high speed [1, 2]. During the entry, the fluid piles up at the intersection between the solid and the free surface, called pile-up region, and a spray jet forms. The fluid velocity is maximized in the pile-up and spray jet, where most of the impact energy is transferred [3]. The large velocity attained in the pile-up region is responsible for a concurrent increase in the fluid pressure with respect to the fluid bulk.

Water entry problems are typically dominated by inertia, so that gravity, viscosity, compressibility, and surface tension can be neglected to a first degree of approximation, as shown in several studies [2]. For example, computational simulations by Facci and Ubertini [4] have investigated the roles of viscosity and gravity, through pertinent Reynolds and Froude numbers, on the physics of impact of a rigid wedge. Campana et al. [5] studied compressibility effects in water entry of wedges and cylinders, and Vella and Metcalfe [6] investigated the extent of surface tension effects on water entry of small-scale objects. Notwithstanding the possibility of neglecting these secondary phenomena with respect to inertia, a full understanding of water entry remains elusive.

The most studied instance of water entry is constituted by hull slamming of marine vessels [2, 7], which has been the object of intense scrutiny since the seminal studies of von Karman [8] and Wagner [9] early last century. In fact, the repeated entry of the hull of a vessel on the water surface induces persistent, large impulsive loadings on the structure, which could reduce the lifetime of the vessel and hinder its maneuverability [1]. Beyond nautical engineering, instances of water entry are routinely found in engineering and life science, such as water landing of crew capsules and seaplanes in aerospace engineering [10], plunging and diving of seabirds [11], and basilisk lizards running on water [12].

This vast array of applications has fueled a large number of experimental and theoretical studies. Building on the classical work of von Karman [8] and Wagner [9], the community has made significant progress in the experimental quantification [13–15] and theoretical prediction of the impact [2, 16]. For example, we have recently seen breakthroughs in understanding how the elastic compliance of the solid could help modulate the hydrodynamic loading [17, 18]. Similarly, recent findings have brought about new insight on the role of the shape of the impacting body, hinting at the possibility of optimal shape design with respect to the hydrodynamic loading and energy transfer [19, 20].

In all these studies, the impacting body is considered as the sole solid object that interacts with the fluid, leaving untouched an entire field of investigation. The need to contemplate the presence of obstacles in the fluid is evident in the study of marine vessels that maneuver in occluded waters and seabirds that plunge and dive close to rocks or ice. In principle, these obstacles could sympathetically interact with the entering body, thereby transforming the physics of the impact.

The notion of sympathetic interactions between solids immersed in fluids is ubiquitous in applied physics, ranging from hydrodynamic coupling of vibrating beams [21, 22], implosion of cylindrical shells in confining tubes [23], and fish swimming in tandem [24]. The complexity of the hydrodynamic coupling often results in unexpected outcomes.

* mporfiri@nyu.edu

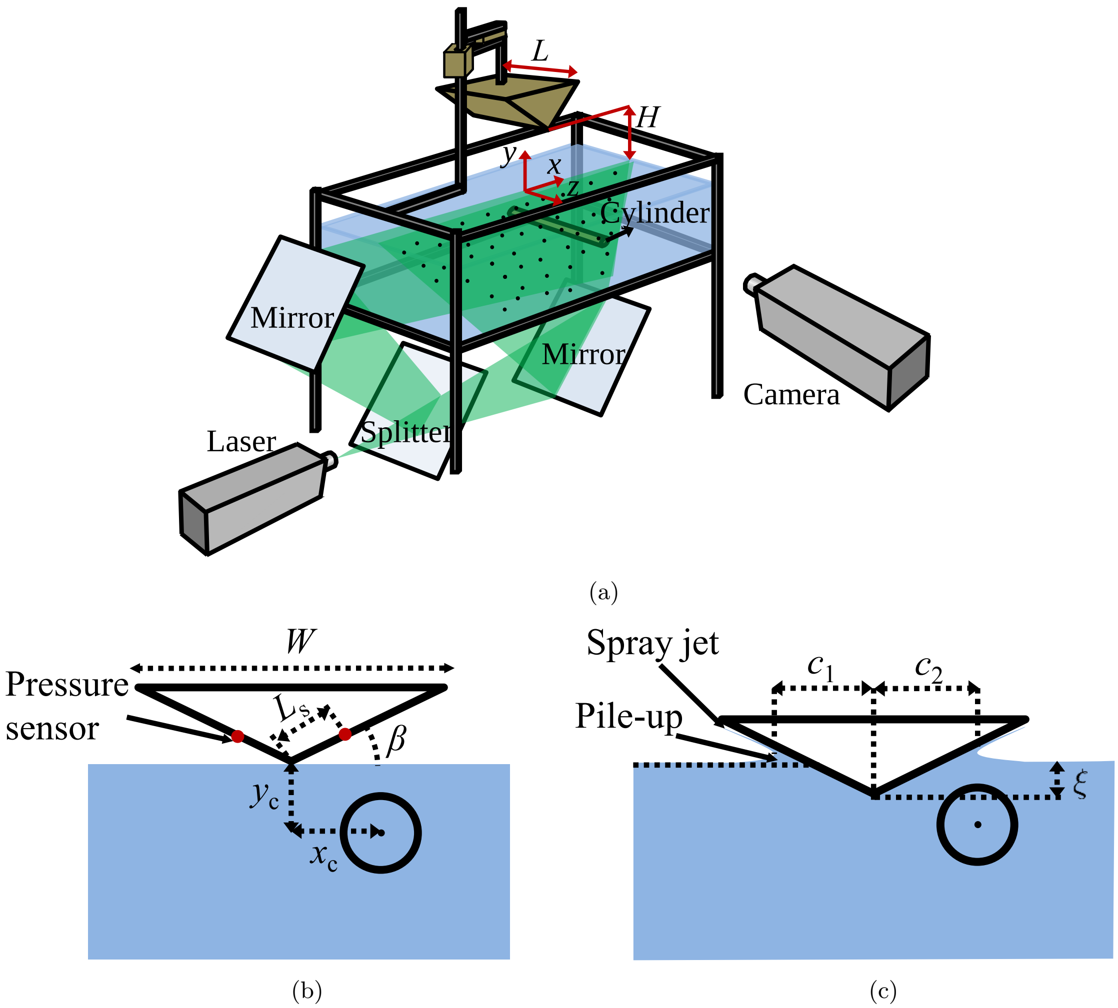

FIG. 1: Schematics of the problem and definition of significant quantities: (a) experimental apparatus and data acquisition system; wedge, fluid, and cylinder at (b) the onset of the impact (red markers label the location of the pressure sensors); and (c) few milliseconds into the entry.

For example, results by Khalid et al. [24] have shown a surprising inverted drag advantage for the leading fish over the following one.

In this paper, we delve into sympathetic interactions during water entry. Specifically, we experimentally study the water entry of a rigid wedge in the presence of a neutrally-buoyant cylinder below the water surface. Particle image velocimetry (PIV) is performed at the mid-span of the wedge where three-dimensional effects are minimal [25]. These measurements are synergistically combined with direct readings via an array of sensors, toward a comprehensive characterization of the fluid-structure interaction. Informed by experimental observations, we establish a potential flow solution based on the modified Logvinovich model (MLM) [26, 27], which offers an improvement of the classical Wagner theory for wedges of moderate deadrise angle.

II. EXPERIMENTS

A. Experimental setup and data analysis

The experimental setup used in this study is equivalent to the one described in [28]. Here, we briefly describe the main features of the setup, consisting of a custom-made apparatus and a data acquisition system. The apparatus comprises a water tank of dimensions $800 \times 320 \times 350$ mm, an aluminum frame that holds the tank 800 mm above the floor, and a free-fall mechanism to release the wedge. Specifically, the mechanism includes a 1.5 m vertical aluminum rail and a carriage system. The carriage system consists of a cart that runs along the rail and an aluminum arm rigidly attached to the cart. The system is connected to a wedge-shaped specimen with length $L = 190\,\mathrm{mm}$, width $W = 200\,\mathrm{mm}$, and deadrise angle $\beta = 37^\circ$ which symmetrically impacts the water surface, see Fig. 1. The total dry mass of the impacting body, which includes the carriage system and wedge, is $M_\mathrm{t} = 0.89\,\mathrm{kg}$. Through a magnet, the impacting body is held at the desired height of $H = 500\,\mathrm{mm}$.

The data acquisition system consists of planar PIV setup and an array of sensors that are embedded in the wedge and apparatus. Briefly, the sensors include one potentiometer that estimates the wedge entry depth ξ, two accelerometers (one capacitive and one piezoelectric) that measure the acceleration during free-fall and impact, and two pressure sensors that are symmetrically placed at a distance L_s from the wedge keel, along the oblique sides of the wedge, see Fig. 1. The acquisition frequency of the PIV system and the sensors are set to 6 kHz and 10 kHz, respectively.

The presence of the cylinder in the fluid causes a large shadow in its trail, if the laser sheet only arrives from one direction. To mitigate this effect, the laser sheet is divided into two sheets of equal power through a rectangular splitter that is mounted below the water tank. Each of the sheets is then reflected on the measurement plane via two mirrors, one installed below the tank and the other on the side, see Fig. 1(a). Polyamide seeding particles of $50\,\mu\mathrm{m}$ in diameter are used as PIV tracers.

The cylinder (radius of $R = 20\,\mathrm{mm}$ and length of 150 mm) is fabricated by a resin casting process to control for its density. Based on preliminary experiments, we found that the obtained specific gravity of 1.01 is sufficient for considering the cylinder to be neutrally buoyant, since its average sinking velocity is 30 times less than wedge entry velocity $V_0 = 3.07\,\mathrm{m/s}$. Neutral buoyancy is herein relevant since we aim at mitigating experimental confounds associated with gravity effects, such that the motion of the cylinder could be univocally related to its sympathetic interaction with the entering wedge.

Data acquisition is initiated when the wedge is released through the magnet. Experiments are performed at room temperature and repeated three times. A maximum of 90 PIV frames are stored for a total of 15 ms of recording. During the wedge free-fall, the cylinder slowly sinks until it reaches an averaged vertical location $y_\mathrm{c} = 28.7\,\mathrm{mm}$ at the onset of the impact, set to $t = 0$. Similar to Russo et al. [28], the velocity of the wedge is estimated by integrating the accelerometers reading.

To quantify the cylinder's effect on the flow physics, we measure the velocity field by processing the PIV images using the open source MATLAB GUI PIVLab [29]. Similar to our previous work [15], we perform a masking procedure that excludes the area above the water surface, the wedge, and the cylinder from PIV processing. The mask also serves to estimate the left c_1 and right c_2 wetted widths.

In addition, PIV images are analyzed via Xcitex ProAnalyst software (www.xcitex.com) to track two points on the cylinder and estimate its motion as the average of the two. This provides the horizontal, x_c, and vertical, y_c, coordinates of the cylinder in time.

B. Results

By comparing the measured displacement ξ, velocity $\dot{\xi}$, and acceleration $\ddot{\xi}$ with those presented in [28], see Fig. 2, we do not notice any effect of the cylinder presence on the wedge motion. Results are averaged across the repetitions and presented along with their standard deviations. Figure 2 demonstrates that the influence of the cylinder on the wedge kinematics is negligible, whereby the results of the new experiments presented in this study closely follow the results in [28] until the wedge touches the cylinder. After the wedge touches the cylinder, at $t = 13.5\,\mathrm{ms}$ into the entry, we register large fluctuations in the acceleration data.

We present the PIV velocity field in Fig. 3(a). The results correspond to the fluid velocity field overlaid with the contours of the velocity magnitude at $t = 7.5\,\mathrm{ms}$. The presence of the cylinder creates a confined flow between the wedge and the cylinder, causing an asymmetric velocity distribution with respect to the wedge keel. In contrast with expectations, we do not register an increase in the velocity field on the right-hand-side (where the cylinder should confine the fluid) with respect to the left-hand-side. Such expectations would be based on previous results on shallow water entry [31, 32] and vibrations of structures close to confining walls [33, 34], which have shown that fluid confinement results in an increase of the velocity. But, our results display a surprising decrease on the right-hand side, due to the presence of the cylinder.

Such a unexpected disturbance in the velocity distribution was echoed by an equivalently surprising distribution for the hydrodynamic loading experienced by the wedge. Specifically, the pressure time-histories at the locations of the pressure sensors installed at $L_\mathrm{s} = 47\,\mathrm{mm}$ on the two sides of the wedge, shown in the top row of Fig. 3(b), indicate that the hydrodynamic loading is lower on the cylinder side until the wedge touches the cylinder at 13.5 ms into the entry. At the onset of the impact, we observe large fluctuations in the pressure loading, but until then, a clear reduction of the pressure due to the cylinder is registered. Interestingly, the observed asymmetry in the pressure

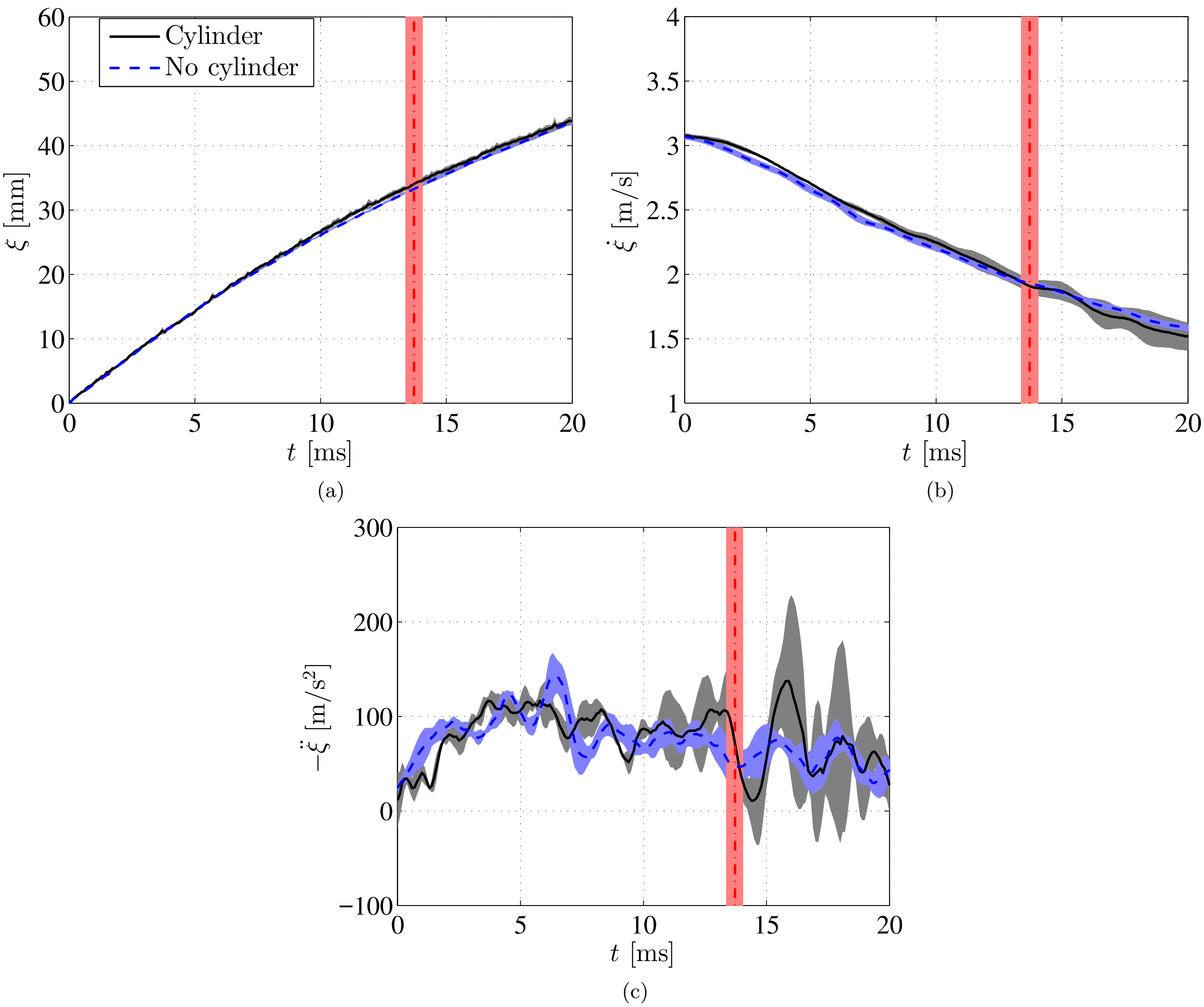

FIG. 2: (a) Entry depth ξ, (b) velocity $\dot{\xi}$, and (c) acceleration $\ddot{\xi}$ of the wedge from experiments in the presence (solid black) and in the absence (dashed blue) of the cylinder (results reproduced from [28]) as functions of time. The time instant of the contact between the wedge and the cylinder is highlighted by a vertical red line. Results are averaged across repetitions and presented with their corresponding standard deviations.

does not manifest into a change of the total force experienced by the wedge with respect to our previous experiments in [28] in the absence of the cylinder, as can be seen from acceleration data in Fig. 2.

The physical underpinning of our unexpected findings should be sought in the presence of the free surface, which makes the water entry problem fundamentally different from previous studies on the dynamics of structures close to confining walls [33, 34] or vibrating in close proximity to each other [21, 22]. These studies would in fact posit an increase in the pressure with the inverse of the distance between the wedge and the cylinder. Previous studies on shallow water entry [31, 32] would also support this hypothesis, but the finite extent of the cylinder with respect to a theoretically infinite bottom wall induces a difference between the problems.

For further insight, we display the location of the cylinder in Fig. 4(a). Based on these findings, we conclude that the cylinder does not appreciably move vertically during the impact. On the other hand, a more noticeable horizontal displacement is observed due to the hydrodynamic loading from the fluid. However, in comparison to the wedge, the cylinder movement is an order of magnitude smaller. Thus, to a first degree of approximation, it is tenable to hypothesize that the cylinder remains stationary during impact.

Also, we track two points on the cylinder to estimate its rotation as the change of the angle $\Delta\theta$ between them from

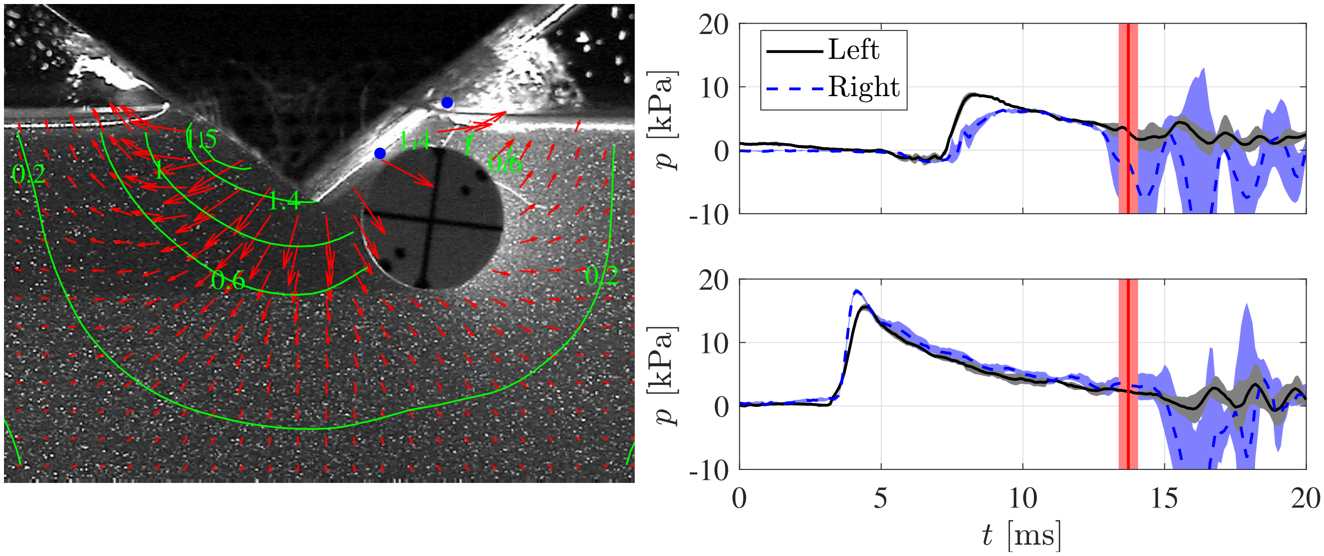

(a) (b)

FIG. 3: (a) PIV images overlaid with velocity vectors and contour plot of the velocity magnitude in m/s at 7.5 ms; the blue markers identify the location of the pressure sensors on the right-hand side of the wedge. (b) Pressure time-histories at the locations of the pressure sensors at $L_{\mathrm{s}} = 22\,\mathrm{mm}$ (bottom) and 47 mm (top) [30]. The time instant of the contact between the wedge and the cylinder is highlighted by a vertical red line. Note that the results in (b) are averaged across the repetitions and presented with their corresponding standard deviations.

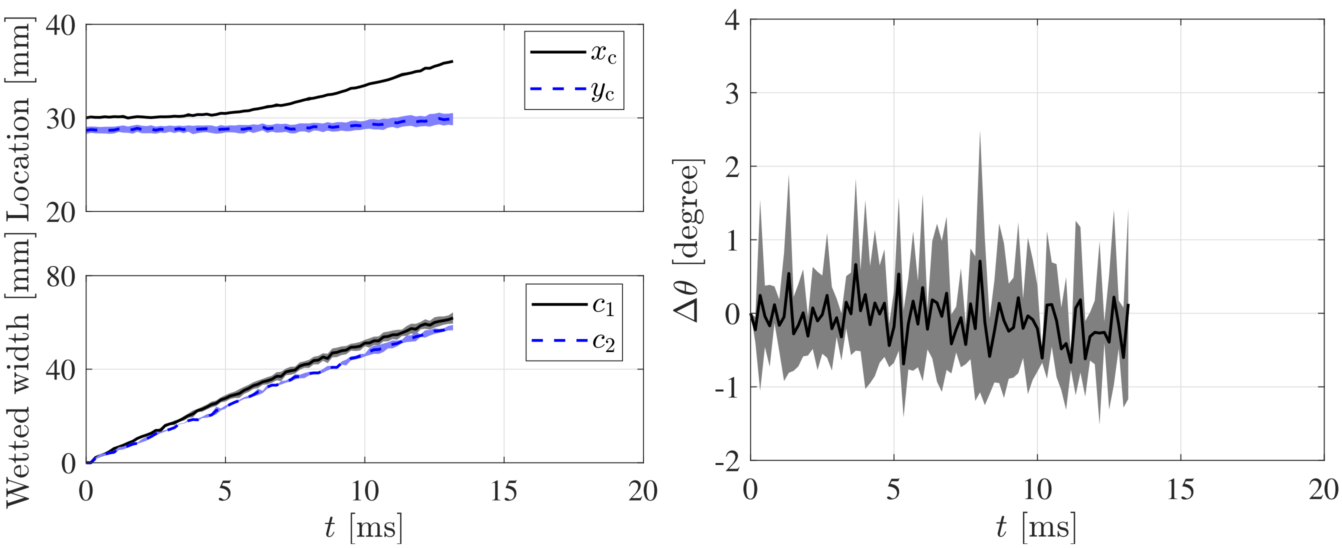

(a) (b)

FIG. 4: (a) Horizontal x_{c} and vertical y_{c} coordinates of the cylinder (top) and time-histories of the left c_1 and right c_2 wetted widths (bottom). (b) Rotation of the cylinder during impact. Note that the results in (a) and (b) are averaged across the repetitions and presented with their corresponding standard deviations.

the initial configuration. The results in Fig. 4(b) display that the cylinder does not rotate throughout the impact, suggesting that it experiences a negligible torque during entry. The time-histories of c_1 and c_2 indicate that the wetted widths closely follow each other throughout the whole duration of the impact, with c_2 being slightly smaller. This may indicate that the presence of the cylinder influences the spatio-temporal evolution of the pile-up on the right-hand side of the wedge, as also evidenced by the pressure measurements in Fig. 3(b).

As displayed in Fig. 3(a), the sensors at $L_{\mathrm{s}} = 47\,\mathrm{mm}$ are outside the confined flow region between the wedge and the cylinder, in the initial stage of the entry. To offer insight into the hydrodynamic loading within this confined flow region, we perform another set of measurements (five repetitions) using two pressure sensors at $L_\mathrm{s} = 22\,\mathrm{mm}$, see the bottom row of Fig. 3(b). In agreement with our original expectations, we register an increase of pressure on the right-hand side of the wedge. Besides a higher peak value, the pressure is slightly larger on the right-hand side, suggesting that the fluid confinement is, in fact, responsible for an increase in the pressure, albeit restricted to the confined region between the wedge and cylinder. This increase in pressure is, in turn, accompanied by the reduction in the hydrodynamic loading away from the confinement region.

III. THEORETICAL EXPLANATION

Overall, our experimental results offer compelling evidence that the cylinder, albeit nearly stationary, influences the physics of the impact, and it does so in a rather complex manner. A possible explanation for this empirical evidence could be proposed based on the classical added mass explanation, first presented by von Karman [8]. On the right-hand side where the cylinder is present, a lesser amount of water is displaced during the impact, thereby reducing the pressure experienced by the wedge. While a simplistic added mass explanation might predict the decrease in the pile-up, it would not suffice to predict the contradictory increase toward the keel.

Toward a principled analysis of the fluid-structure interaction, we propose a theoretical formulation based on the MLM model, which describes the fluid flow within a two-dimensional potential flow theory and solves for the pressure by retaining second-order nonlinearities in the Bernoulli equation [26, 27]. Compared to Wagner's solution [9], the MLM allows for the study of moderately large deadrise angles, compatible with our experiments.

A key step in the implementation of the MLM is the solution of the mixed boundary value problem resulting from the presence of the cylinder in the fluid. Toward an accurate description of the experiment, we account for the motion of the cylinder from Fig. 4(a). In addition, we consider the left and right wetted widths to be different, and compute them as part of the solution. A boundary integral representation of the velocity potential is obtained through the method of Green's functions [35], which we numerically solve using the Weierstrass approximation theorem with Legendre polynomials as basis functions. Details of the MLM formulation is discussed in what follows.

A. Modeling framework

Within the MLM approach, neglecting gravity, viscosity, compressibility, and surface tension effects, the pressure profile on the wetted portion of the wedge is obtained through the nonlinear Bernoulli equation [27, 28]

$$p(x, y_\mathrm{w}(x,t), t) = -\rho_\mathrm{f}\left(\left.\frac{\partial\phi(x,y,t)}{\partial t}\right|_{y=0} - \ddot{\xi}(t)\left(|x|\tan\beta - \xi(t)\right) + \frac{1}{2}\frac{1}{1+\tan^2\beta}\left(\left.\frac{\partial\phi(x,y,t)}{\partial x}\right|_{y=0}\right)^2 + \frac{1}{2}\dot{\xi}^2(t)\right), \tag{1}$$

where ρ_f is the fluid density, ϕ is the velocity potential obtained via Wagner formulation, and $y_\mathrm{w} = |x|\tan\beta - \xi$ is the position of the wedge at time t. The first two terms on the right-hand side of Eq. (1) relate to the pressure from the unsteady portion of the flow, while the remaining two are associated with the dynamic pressure.

Within Wagner theory, we linearize the boundary conditions for the velocity potential which are imposed on the undisturbed free surface at $y = 0$, such that we arrive at the following mixed boundary value problem:

$$\Delta\phi(x,y,t) = 0, \tag{2a}$$

$$\frac{\partial\phi(x,y,t)}{\partial y} = \frac{\partial y_\mathrm{w}(x,t)}{\partial t}, \qquad y = 0 \text{ and } -c_1(t) < x < c_2(t), \tag{2b}$$

$$\frac{\partial\phi(x,y,t)}{\partial \mathbf{n}} = \mathbf{v}_\mathrm{c}(t)\cdot\mathbf{n}, \qquad R = \sqrt{(x - x_\mathrm{c}(t))^2 + (y + y_\mathrm{c}(t))^2}, \tag{2c}$$

$$\phi(x,y,t) = 0, \qquad y = 0 \text{ and } x < -c_1(t),\ x > c_2(t), \tag{2d}$$

$$\phi(x,y,t) \to 0, \qquad y \to -\infty \text{ and } x \to \infty, \tag{2e}$$

where Δ is the Laplace operator, $\mathbf{n}$ is the inward unit normal to the cylinder, $\mathbf{v}_\mathrm{c}(t) = (\dot{x}_\mathrm{c}(t), \dot{y}_\mathrm{c}(t))$ is the cylinder velocity, c_1 and c_2 are the left and right wetted widths, respectively, and a dot indicates inner product. Irrotationality and incompressibility of the flow are imposed through Eq. (2a); Eqs. (2b) and (2c) enforce the no-penetration boundary condition on the wetted portion of the wedge and on the immersed cylinder, respectively; the pressure is set to zero on the undisturbed free surface through Eq. (2d); and Eq. (2e) indicates that the flow is at rest far away from the entry region.

By defining the nondimensional coordinates $\hat{x} = x/a_1 + a_2$ and $\hat{y} = -y/a_1$, where $a_1 = (c_1 + c_2)/2$ and $a_2 = (c_1 - c_2)/(c_1 + c_2)$, we transform the mixed boundary value problem into

$$\begin{aligned}
&\Delta\phi(\hat{x},\hat{y},t) = 0, && && \text{(3a)}\\
&\frac{\partial\phi(\hat{x},\hat{y},t)}{\partial\hat{y}} = a_1(t)\dot{\xi}(t), && \hat{y}=0 \text{ and } |\hat{x}|<1, && \text{(3b)}\\
&\frac{\partial\phi(\hat{x},\hat{y},t)}{\partial\mathbf{n}} = a_1(t)\left(\mathbf{v}_\mathrm{c}(t)\cdot\mathbf{n}\right), && \hat{R}(t) = \sqrt{(\hat{x}-\hat{x}_\mathrm{c}(t))^2 + (\hat{y}-\hat{y}_\mathrm{c}(t))^2}, && \text{(3c)}\\
&\phi(\hat{x},\hat{y},t) = 0, && \hat{y}=0 \text{ and } |\hat{x}|>1, && \text{(3d)}\\
&\phi(\hat{x},\hat{y},t) \to 0, && \hat{y}\to-\infty \text{ and } \hat{x}\to\infty, && \text{(3e)}
\end{aligned}$$

where $\hat{R} = R/a_1$, $\hat{x}_\mathrm{c} = x_\mathrm{c}/a_1 + a_2$, and $\hat{y}_\mathrm{c} = y_\mathrm{c}/a_1$.

We establish a solution of the mixed boundary value problem in Eq. (3) through the theory of Green's functions. Specifically, we define the Green's function $g(\hat{x}_\mathrm{c},\hat{y}_\mathrm{c},\hat{R},\hat{x},\hat{y}|\zeta,\eta)$ as the solution of the following mixed boundary value problem [35, 36]:

$$\begin{aligned}
&\Delta g(\hat{x}_\mathrm{c}(t),\hat{y}_\mathrm{c}(t),\hat{R}(t),\hat{x},\hat{y}|\zeta,\eta) = -\delta(\hat{x}-\zeta)\delta(\hat{y}-\eta), && && \text{(4a)}\\
&g(\hat{x}_\mathrm{c}(t),\hat{y}_\mathrm{c}(t),\hat{R}(t),\hat{x},\hat{y}|\zeta,\eta) = 0, && \hat{y}=0 && \text{(4b)}\\
&\frac{\partial g(\hat{x}_\mathrm{c}(t),\hat{y}_\mathrm{c}(t),\hat{R}(t),\hat{x},\hat{y}|\zeta,\eta)}{\partial\mathbf{n}} = 0, && \hat{R}(t) = \sqrt{(\hat{x}-\hat{x}_\mathrm{c}(t))^2 + (\hat{y}-\hat{y}_\mathrm{c}(t))^2}, && \text{(4c)}\\
&g(\hat{x}_\mathrm{c}(t),\hat{y}_\mathrm{c}(t),\hat{R}(t),\hat{x},\hat{y}|\zeta,\eta) \to 0, && \hat{y}\to-\infty \text{ and } \hat{x}\to\infty. && \text{(4d)}
\end{aligned}$$

The solution of Eq. (3) is then obtained by substituting the Green's function from Eq. (4) into Eq. (6.0.13) in [35], see also Example 1.1.4 in [36], to arrive at

$$\begin{aligned}
\phi(\hat{x},\hat{y},t) = &\int_{-1}^{1} \phi(\zeta,0,t)\left.\frac{\partial g(\hat{x}_\mathrm{c}(t),\hat{y}_\mathrm{c}(t),\hat{R}(t),\hat{x},\hat{y}|\zeta,\eta)}{\partial\eta}\right|_{\eta=0} \mathrm{d}\zeta\\
&-\int_{-\pi}^{\pi} a_1(t)\hat{R}(t)\left(\dot{x}_\mathrm{c}(t)\cos\alpha + \dot{y}_\mathrm{c}(t)\sin\alpha\right) g(\hat{x}_\mathrm{c}(t),\hat{y}_\mathrm{c}(t),\hat{R}(t),\hat{x},\hat{y}|\hat{R}(t)\cos\alpha,\hat{R}(t)\sin\alpha)\ \mathrm{d}\alpha,
\end{aligned} \tag{5}$$

where α is measured counterclockwise from the horizontal axis $\hat{x}$. Eq. (5) demonstrates that the knowledge of the velocity potential on the wetted wedge is sufficient to compute the fluid flow everywhere, through an integration involving the Green's function. The pressure in the MLM formulation in Eq. (1) is also determined upon knowledge of $\phi(\hat{x},0,t)$. We seek to find $\phi(\hat{x},0,t)$ in Eq. (5) through the boundary condition in Eq. (3b); substitution of Eq. (5) into Eq. (3b) yields the following integral equation for $\phi(\hat{x},0,t)$

$$\begin{aligned}
a_1(t)\dot{\xi}(t) = &\int_{-1}^{1} \phi(\zeta,0,t)\left.\frac{\partial^2 g(\hat{x}_\mathrm{c}(t),\hat{y}_\mathrm{c}(t),\hat{R}(t),\hat{x},\hat{y}|\zeta,\eta)}{\partial\hat{y}\partial\eta}\right|_{\eta=0,\ \hat{y}=0} \mathrm{d}\zeta\\
&-\int_{-\pi}^{\pi} a_1(t)\hat{R}(t)\left(\dot{x}_\mathrm{c}(t)\cos\alpha + \dot{y}_\mathrm{c}(t)\sin\alpha\right)\left.\frac{\partial g(\hat{x}_\mathrm{c}(t),\hat{y}_\mathrm{c}(t),\hat{R}(t),\hat{x},\hat{y}|\hat{R}(t)\cos\alpha,\hat{R}(t)\sin\alpha)}{\partial\hat{y}}\right|_{\hat{y}=0} \mathrm{d}\alpha.
\end{aligned} \tag{6}$$

The details to determine the Green's function as the solution of the mixed boundary value problem in Eq. (4) is summarized in Appendix A.

The unknowns a_1 and a_2 are yet to be determined to achieve complete closure of the formulation. These unknowns, which depend on the wetted widths c_1 and c_2, might be found using the Wagner condition [37]. This condition states that the free surface elevation should match the body profile at c_1 and c_2, that is,

$$\left. y_\mathrm{w}(x,t)\right|_{x=c_1(t),-c_2(t)} = -\frac{1}{a_1(t)}\int_0^t \left.\frac{\partial\phi(x/a_1(\tau)+a_2(\tau),\hat{y},t)}{\partial\hat{y}}\right|_{\hat{y}=0,x=c_1(t),-c_2(t)} \mathrm{d}\tau. \tag{7}$$

The complexity of the formulation does not permit the direct use of Eq. (7) due to the temporal integration involved. To obviate this difficulty, we define a displacement potential, following [38, 39],

$$\psi(x,y,t)=\int_0^t \phi(x,y,t)\ \mathrm{d}\tau, \tag{8}$$

and solve the complementary boundary value problem for ψ

$$\begin{aligned}
&\Delta\psi(x,y,t)=0, && && (9\text{a})\\
&\frac{\partial\psi(x,y,t)}{\partial y}=y_{\mathrm{w}}(x,t), && y=0 \text{ and } -c_1(t)<x<c_2(t), && (9\text{b})\\
&\frac{\partial\psi(x,y,t)}{\partial \mathbf{n}}=\mathbf{l}_{\mathrm{c}}(t)\cdot\mathbf{n}, && R=\sqrt{(x-x_{\mathrm{c}}(t))^2+(y+y_{\mathrm{c}}(t))^2}, && (9\text{c})\\
&\psi(x,y,t)=0, && y=0 \text{ and } x<-c_1(t),\ x>c_2(t), && (9\text{d})\\
&\psi(x,y,t)\to 0, && y\to-\infty \text{ and } x\to\infty, && (9\text{e})
\end{aligned}$$

where $\mathbf{l}_{\mathrm{c}}(t)=(l_x,l_y)$, and $l_x=x_{\mathrm{c}}(t)-x_{\mathrm{c}}(0)$ and $l_y=y_{\mathrm{c}}(t)-y_{\mathrm{c}}(0)$ are the horizontal and vertical components of the cylinder displacement, respectively. Changing to nondimensional coordinates, we establish

$$\begin{aligned}
&\Delta\psi(\hat{x},\hat{y},t)=0, && && (10\text{a})\\
&\frac{\partial\psi(\hat{x},\hat{y},t)}{\partial \hat{y}}=-a_1(t)y_{\mathrm{w}}(\hat{x},t), && \hat{y}=0 \text{ and } |\hat{x}|<1, && (10\text{b})\\
&\frac{\partial\psi(\hat{x},\hat{y},t)}{\partial \mathbf{n}}=a_1(t)\left(\mathbf{l}_{\mathrm{c}}(t)\cdot\mathbf{n}\right), && \hat{R}(t)=\sqrt{(\hat{x}-\hat{x}_{\mathrm{c}}(t))^2+(\hat{y}-\hat{y}_{\mathrm{c}}(t))^2}, && (10\text{c})\\
&\psi(\hat{x},\hat{y},t)=0, && \hat{y}=0 \text{ and } |\hat{x}|>1, && (10\text{d})\\
&\psi(\hat{x},\hat{y},t)\to 0, && \hat{y}\to-\infty \text{ and } \hat{x}\to\infty. && (10\text{e})
\end{aligned}$$

Solution of the boundary value problem in Eq. (10) can be undertaken within the same framework introduced to solve ϕ. Specifically, by utilizing the Green's function theorem, we arrive at

$$\begin{aligned}
-a_1(t)y_{\mathrm{w}}(\hat{x},t)=&\int_{-1}^{1}\psi(\zeta,0,t)\left[\frac{1}{\pi(\hat{x}-\zeta)^2}+\left.\frac{\partial^2 g_{\mathrm{c}}(\hat{x}_{\mathrm{c}}(t),\hat{y}_{\mathrm{c}}(t),\hat{R}(t),\hat{x},\hat{y}|\zeta,\eta)}{\partial\hat{y}\partial\eta}\right|_{\eta=0,\ \hat{y}=0}\right]\mathrm{d}\zeta\\
&-\int_{-\pi}^{\pi}a_1(t)\hat{R}(t)\left(l_x\cos\alpha+l_y\sin\alpha\right)\left[\left.\frac{\partial g_{\mathrm{w}}(\hat{x},\hat{y}|\hat{R}(t)\cos\alpha,\hat{R}(t)\sin\alpha)}{\partial\hat{y}}\right|_{\hat{y}=0}\right.\\
&\left.+\left.\frac{\partial g_{\mathrm{c}}(\hat{x}_{\mathrm{c}}(t),\hat{y}_{\mathrm{c}}(t),\hat{R}(t),\hat{x},\hat{y}|\hat{R}(t)\cos\alpha,\hat{R}(t)\sin\alpha)}{\partial\hat{y}}\right|_{\hat{y}=0}\right]\mathrm{d}\alpha.
\end{aligned}\tag{11}$$

By construction, ψ does not have singularities at the jet root locations c_1 and c_2, unlike ϕ; therefore, Wagner condition for this problem reduces to the determination of the wetted widths for which the displacement is finite at the jet roots [38, 39]. Since $\psi(\hat{x},0,t)=0$ on the free surface, it is trivial that

$$\left.\frac{\partial\psi(\hat{x},0,t)}{\partial\hat{x}}\right|_{\hat{x}=\pm1}=0. \tag{12}$$

Although the current formulation allows for the simultaneous computation of the wedge and cylinder motion through the use of Newton's second law of motion, we have opted to use experimental data of the wedge and cylinder motion to avoid confounds in the calculation of the hydrodynamic loading. The details of the semi-analytical treatment of the mathematical model are presented in Appendix B. We input the experimental time-traces of the wedge and cylinder motion, as well as their derivatives into the MLM formulation and take $\rho_{\mathrm{f}}=1000\,\mathrm{kg/m^3}$ to estimate the loading from Eq. (1). More specifically, we solve the following equations: Eqs. (B4), (B9), (B15), and (B16). To compute the velocity and acceleration of the cylinder from experimental data (horizontal l_x and vertical l_y), we fit the horizontal and vertical displacements with linear functions in χ, where $\chi = \xi - V_0 t$.

Upon estimating the slope from fitting, the velocity and acceleration are readily evaluated from the wedge motion and entry speed. The feasibility of a linear approximation for the cylinder motion with respect to χ rests upon the loading exerted by the fluid on the cylinder, which should be a linear function of the wedge acceleration, due to hydrodynamic coupling. Figure 5 confirms the validity of the proposed fit. Finally, we comment that the accuracy of the numerical approach presented in this Appendix was checked against original Wagner's solution when the cylinder is absent.

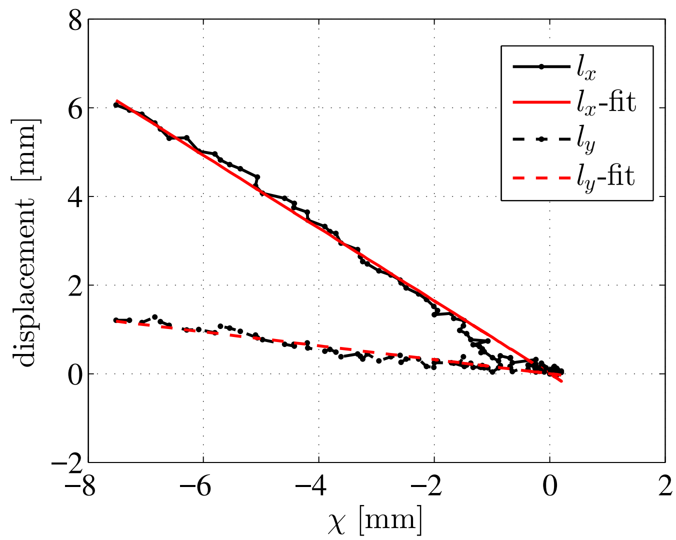

FIG. 5: Experimental results for the horizontal l_x and vertical l_y cylinder displacements versus χ, together with their corresponding linear fits.

B. Results

The estimated time histories of c_1 and c_2 from the MLM formulation, along with their derivatives, $\dot{c}_1$ and $\dot{c}_2$, are shown in Fig. 6(a). Theoretical predictions on the wetted width are in agreement with experimental data in Fig. 4(a), whereby c_1 and c_2 closely follow each other throughout the impact, with c_2 taking smaller values at the end. The rate of change of the right wetted width $\dot{c}_2$ displays an interesting behavior: at the beginning of the impact, $\dot{c}_2$ closely follows $\dot{c}_1$, but from $t = 2$ to $4.5\,\mathrm{ms}$ it takes slightly higher values, before dropping below $\dot{c}_1$ for the rest of the impact. This behavior evidences the influence of the cylinder on the spatio-temporal evolution of the pile-up on the right-hand side of the wedge. Based on these findings, we expect that the presence of the cylinder should have an important role on the hydrodynamic loading distribution. In fact, in the MLM formulation, the hydrodynamic loading is proportional to the rate of the change of the wetted widths $\dot{c}_1$ and $\dot{c}_2$. Therefore, the predicted difference between $\dot{c}_1$ and $\dot{c}_2$ should translate into a tangible difference between the left- and right-hand side loadings, especially in the pile-up regions, as also seen from experiments in Fig. 4.

Such a difference is demonstrated in Fig. 6(b), where we display predictions on the pressure profiles on the entire wetted width of the wedge at three time instants. The pressure on the right-hand side at $t = 4\,\mathrm{ms}$ is higher than that on the left-hand side, which may be ascribed to the larger $\dot{c}_2$ values found in Fig. 6(a). After $t = 4.5\,\mathrm{ms}$, the pressure profiles display a consistent decrease in the right pile-up with respect to the left pile-up, in agreement with the predicted decrease of $\dot{c}_2$ beyond this time instant. However, the pressure in the proximity of the keel, in the confined region between the wedge and the cylinder, still attains larger values than the left-hand side. Thus, after $t = 4.5\,\mathrm{ms}$, pressure variations close to the keel offset the differences in the two pile-ups, resulting in a secondary change in the force resultant on the right-hand side of the wedge. Such a counterbalancing effect explains the modest change of the overall motion of the wedge due to the cylinder. From $t = 2$ to $4.5\,\mathrm{ms}$, the force resultant on the right-hand side is higher than the left-hand side, but values are not sufficiently large to elicit a change in the motion of the wedge.

The MLM is also successful in qualitatively anticipating the time evolution of the pressure at $L_\mathrm{s} = 22$ and $47\,\mathrm{mm}$, with respect to experimental observations. More specifically, the MLM predicts an increase in the pressure on the

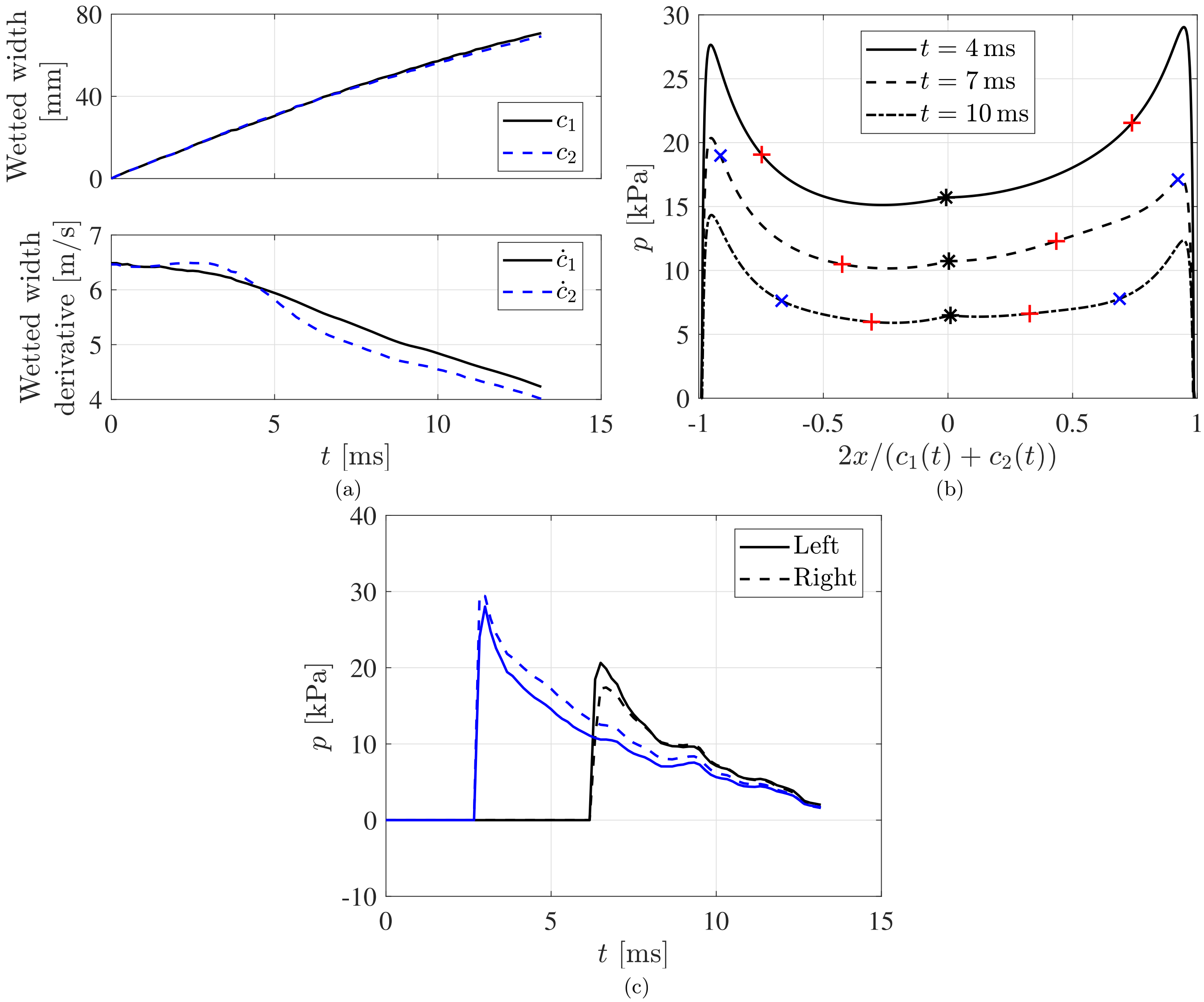

FIG. 6: (a) Time-histories of the left c_1 and right c_2 wetted widths (top) and their derivatives $\dot{c}_1$ and $\dot{c}_2$ (bottom) from MLM. (b) Pressure profile on the wedge wetted surface from MLM; the location of the keel and the pressure sensors are highlighted by * (keel), + (sensors at $L_\mathrm{s} = 22\,\mathrm{mm}$), and $\times$ (sensors at $L_\mathrm{s} = 47\,\mathrm{mm}$). (c) Pressure time-histories at $L_\mathrm{s} = 22\,\mathrm{mm}$ (blue) and $L_\mathrm{s} = 47\,\mathrm{mm}$ (black) on the left- (solid) and right- (dashed) hand sides of the wedge from MLM.

right-hand side with respect to the left-hand side for the sensors closer to the keel, while it anticipates the opposite trend for the other pair of sensors, see Fig. 6(c). The slight offset of the keel position with respect to the origin in Fig. 6(b) and the modest lag between the pressure time histories in Fig. 6(c) are both related to the difference in the pile-up evolution on the two sides of the wedge, which is incorporated in the MLM.

Based on the MLM results, we identify two key effects of the cylinder. On the one hand, it creates a confined flow in the vicinity of the keel, where pressure increases. On the other hand, its presence decreases the amount of fluid that could be transported to the pile-up, begetting a decrease of the pressure therein. Another factor that may be important in shaping the sympathetic interaction between the wedge and the cylinder is represented by the water jets in the pile-up regions. As shown in [3], in the absence of occluding obstacles, these jets contain most of the energy imparted by the wedge during the impact. It is thus tenable to hypothesize that the cylinder might modulate the velocity and thickness of the jets, ultimately inducing a nonsymmetric distribution of the pressure along the wetted portion of the wedge. However, neither the MLM nor our experimental results can support a detailed study of the physics of the jets. Future work might seek to develop this aspect through direct numerical simulations or detailed flow measurements of the jets.

IV. CONCLUSIONS

In this paper, we analyzed the water entry of a rigid wedge in the presence of a solid cylinder below the water surface. Our study indicates a surprising effect of the presence of the cylinder. While the presence of the cylinder elicits a predictable increase in the pressure close to the keel, it is also responsible for a pressure drop in the vicinity of the pile-up. The unanticipated decrease of pressure can be partially explained through the added mass phenomenon, whereby the presence of the cylinder leads to a reduction in the virtual mass that is displaced by the wedge during its entry. However, this minimalistic model would not suffice to predict the concurrent pressure increase toward the keel.

Further insight into the physics of water entry was obtained with a potential flow solution of the problem, which offered a more precise quantification of the fluid-structure interaction. Based on our theoretical results we identified two key effects of the cylinder. First, the presence of the cylinder creates a confined flow in the vicinity of the keel, where pressure increases. Due to the presence of the cylinder, less amount of fluid is transported to the pile-up, resulting in a decrease of the wetted width and pressure on the side where the cylinder is located.

It is tenable that the water jets, in the pile-up regions, could be important in shaping the sympathetic interaction. However, neither the MLM nor our experimental results support a detailed study of the physics of the jets. Thus, a possible future direction might seek to investigate the effect of the jets through direct numerical simulations or detailed flow measurements. Other possible avenues for future work might entail a distributed measurement of the pressure on the entire wedge, parametric analysis of the geometric and physical factors, and mathematical modeling via a generalized Wagner theory. Increasing the number of pressure sensors on the wedge may be practically difficult due to the complex wiring that would be required. Pressure measurement might instead be simpler through a PIV-based pressure reconstruction technique that extends our previous work [40] to treat a solid object in the fluid domain. These additional data should be collected by systematically varying the initial position of the cylinder with respect to the wedge, as well as their relative size to isolate key nondimensional factors of the fluid-structure interaction. Finally, a generalized Wagner theory could assist in improving our prediction of the pressure distribution on the body profile, by properly addressing nonlinear boundary conditions.

V. ACKNOWLEDGMENT

This research was supported by the Office of Naval Research through grants N00014-10-1-0988 and N00014-18-1-2218.

Appendix A: Green's function

The task here is to determine the Green's function, as the solution of the mixed boundary value problem in Eq. (4). Such a Green's function can be easily constructed using the method of images. Within this approach, additional free-space Green's functions, outside the domain of interest, are subtracted from or added to the free-space Green's function in the domain of interest to define boundaries of Dirichlet ($g = 0$) or Neumann ($\partial g/\partial \mathbf{n} = 0$) type, respectively, see Section 6.2 in [35]. The free-space Green's function for Laplace equation in two dimensions is [35]:

$$g_{\mathrm{fs}}(\hat{x}, \hat{y}|\zeta, \eta) = -\frac{1}{4\pi} \ln\left[(\hat{x} - \zeta)^2 + (\hat{y} - \eta)^2\right]. \tag{A1}$$

Using Eq. (A1), we construct the intended Green's function for Eq. (4) as summarized in the following two steps.

First, we add a free-space Green's function to satisfy the Neumann boundary condition on the cylinder surface using the so-called "inversion with respect to the circle" rule, see Section 6.3 in [35]. Specifically, if we define

$$\rho\left(\hat{x}_{\mathrm{c}}, \hat{y}_{\mathrm{c}}, \hat{R}\right) = \frac{1}{\hat{R}} \sqrt{(\zeta - \hat{x}_{\mathrm{c}})^2 + (\eta - \hat{y}_{\mathrm{c}})^2}, \tag{A2}$$

as the normalized distance between the center of the cylinder and the free-space Green's function source, the added free-space Green's function should be placed at the same line that connects the cylinder's center with the source, but at a normalized distance of $1/\rho$.

The second and final step entails mirroring the Green's function built during the first step with respect to the $\hat{x}$-axis and performing a subtraction to satisfy the Dirichlet boundary condition at $\hat{y} = 0$. Thus, we stablish:

$$g(\hat{x}_{\mathrm{c}}, \hat{y}_{\mathrm{c}}, \hat{R}, \hat{x}, \hat{y}|\zeta, \eta) = \frac{1}{4\pi} \ln \left[\frac{(\hat{x}-\zeta)^2 + (\hat{y}+\eta)^2}{(\hat{x}-\zeta)^2 + (\hat{y}-\eta)^2} \times \frac{\left((\hat{x}-\hat{x}_{\mathrm{c}})\, \rho^2\left(\hat{x}_{\mathrm{c}}, \hat{y}_{\mathrm{c}}, \hat{R}\right) - (\zeta - \hat{x}_{\mathrm{c}})\right)^2 + \left((\hat{y}+\hat{y}_{\mathrm{c}})\, \rho^2\left(\hat{x}_{\mathrm{c}}, \hat{y}_{\mathrm{c}}, \hat{R}\right) + (\eta - \hat{y}_{\mathrm{c}})\right)^2}{\left((\hat{x}-\hat{x}_{\mathrm{c}})\, \rho^2\left(\hat{x}_{\mathrm{c}}, \hat{y}_{\mathrm{c}}, \hat{R}\right) - (\zeta - \hat{x}_{\mathrm{c}})\right)^2 + \left((\hat{y}-\hat{y}_{\mathrm{c}})\, \rho^2\left(\hat{x}_{\mathrm{c}}, \hat{y}_{\mathrm{c}}, \hat{R}\right) - (\eta - \hat{y}_{\mathrm{c}})\right)^2} \right], \tag{A3}$$

where the first fraction in the argument of the logarithm in Eq. (A3) corresponds to the original Green's function of the Wagner formulation with no cylinder present, while the second fraction encapsulates the contribution from the cylinder. We use this property to write the Green's function as the summation of two terms, associated with the wedge and the cylinder, namely,

$$g_{\mathrm{w}}(\hat{x}, \hat{y}|\zeta, \eta) = \frac{1}{4\pi} \ln \left[\frac{(\hat{x}-\zeta)^2 + (\hat{y}+\eta)^2}{(\hat{x}-\zeta)^2 + (\hat{y}-\eta)^2} \right], \tag{A4a}$$

$$g_{\mathrm{c}}(\hat{x}_{\mathrm{c}}, \hat{y}_{\mathrm{c}}, \hat{R}, \hat{x}, \hat{y}|\zeta, \eta) = \frac{1}{4\pi} \ln \left[\frac{\left((\hat{x}-\hat{x}_{\mathrm{c}})\, \rho^2\left(\hat{x}_{\mathrm{c}}, \hat{y}_{\mathrm{c}}, \hat{R}\right) - (\zeta - \hat{x}_{\mathrm{c}})\right)^2 + \left((\hat{y}+\hat{y}_{\mathrm{c}})\, \rho^2\left(\hat{x}_{\mathrm{c}}, \hat{y}_{\mathrm{c}}, \hat{R}\right) + (\eta - \hat{y}_{\mathrm{c}})\right)^2}{\left((\hat{x}-\hat{x}_{\mathrm{c}})\, \rho^2\left(\hat{x}_{\mathrm{c}}, \hat{y}_{\mathrm{c}}, \hat{R}\right) - (\zeta - \hat{x}_{\mathrm{c}})\right)^2 + \left((\hat{y}-\hat{y}_{\mathrm{c}})\, \rho^2\left(\hat{x}_{\mathrm{c}}, \hat{y}_{\mathrm{c}}, \hat{R}\right) - (\eta - \hat{y}_{\mathrm{c}})\right)^2} \right]. \tag{A4b}$$

Here, g_{w} correspond to the wedge contribution while g_{c} to the cylinder. Note that g_{c} is a function of the cylinder position. This decomposition suggests the possibility of considering more than one cylinder by simply summing their corresponding Green's function. Thus, the proposed mathematical framework can be extended to any number of rigid bodies within the fluid domain.

Appendix B: Semi-analytical treatment of the mixed boundary value problem

Upon establishing a closed-form expression for the Green's function in Appendix A, we substitute Eq. (A3) into Eq. (6) to obtain

$$\begin{aligned} a_1(t)\dot{\xi}(t) = &\int_{-1}^{1} \phi(\zeta, 0, t) \left[\frac{1}{\pi(\hat{x}-\zeta)^2} + \left.\frac{\partial^2 g_{\mathrm{c}}(\hat{x}_{\mathrm{c}}(t), \hat{y}_{\mathrm{c}}(t), \hat{R}(t), \hat{x}, \hat{y}|\zeta, \eta)}{\partial \hat{y} \partial \eta}\right|_{\eta=0,\ \hat{y}=0} \right] \mathrm{d}\zeta \\ &- \int_{-\pi}^{\pi} a_1(t)\hat{R}(t) \left(\dot{x}_{\mathrm{c}} \cos\alpha + \dot{y}_{\mathrm{c}} \sin\alpha\right) \left[\left.\frac{\partial g_{\mathrm{w}}(\hat{x}, \hat{y}|\hat{R}(t)\cos\alpha, \hat{R}(t)\sin\alpha)}{\partial \hat{y}}\right|_{\hat{y}=0} \right. \\ &\left. + \left.\frac{\partial g_{\mathrm{c}}(\hat{x}_{\mathrm{c}}(t), \hat{y}_{\mathrm{c}}(t), \hat{R}(t), \hat{x}, \hat{y}|\hat{R}(t)\cos\alpha, \hat{R}(t)\sin\alpha)}{\partial \hat{y}}\right|_{\hat{y}=0} \right] \mathrm{d}\alpha, \end{aligned} \tag{B1}$$

where we have omitted expanding the expressions for g_{c} and g_{w} for brevity.

Unfortunately, due to the presence of the terms stemming from the presence of the cylinder, we could not find a closed form solution. Thus, we present a semi-analytical method to numerically estimate $\phi(\hat{x}, 0, t)$. To this aim, we apply Taylor's theorem and the Weierstrass approximation [41], which asserts that an arbitrary continuous function can be locally approximated by a polynomial function. In a recent study, Cohen and Tan [42] showed that an approximation based on Legendre polynomials might have improved speed and accuracy over Taylor polynomials. Thus, we adopt the Legendre polynomials $P_n(\hat{x})$ as the basis functions for our approximation. Neglecting the presence of the cylinder, the original Wagner velocity potential on $\hat{y} = 0$ is $-a_1(t)\xi(t)\sqrt{1-\hat{x}^2}$. Based on the original solution, we posit that $\phi(\hat{x}, 0, t)$ can be expressed as

$$\phi(\hat{x}, 0, t) = \mathbf{P}^{\mathrm{T}}(\hat{x})\mathbf{s}_1(t)a_1(t)\dot{\xi}(t)\sqrt{1-\hat{x}^2}, \tag{B2}$$

where $\mathbf{s}_1$ and $\mathbf{P}$ are $(N+1)$-dimensional vectors of coefficients and Legendre polynomials, respectively, and superscript T represents matrix transposition. If only one term is considered in Eq. (B2), since $P_0(\hat{x}) = 1$, we recover the original solution by Wagner. To facilitate the computations, we express the vector of Legendre polynomials as

$$\mathbf{P}(\hat{x}) = \mathbf{Q}\mathbf{r}(\hat{x}), \tag{B3}$$

where $\mathbf{r}^{\mathrm{T}}(\zeta) = [\zeta^0, \zeta^1, \zeta^2, \ldots, \zeta^N]$ is $(N+1)$-dimensional vector of polynomials while $\mathbf{Q}$ is an $[(N+1)\times(N+1)]$-dimensional matrix of polynomial coefficients, where the i-th row contains the polynomial coefficients of $P_i(\hat{x})$.

Next, we substitute Eq. (B2) into Eq. (B1), multiply both sides by $\mathbf{P}(\hat{x})$, and integrate from $[-1,1]$ to establish

$$\mathbf{Q}\left(\mathbf{K}_1 + \mathbf{K}_2\left(\hat{x}_{\mathrm{c}}(t), \hat{y}_{\mathrm{c}}(t), \hat{R}(t)\right)\right)\mathbf{Q}^{\mathrm{T}}\mathbf{s}_1(t) = \mathbf{Q}\mathbf{d}_1 + \mathbf{Q}\mathbf{d}_2\left(\hat{x}_{\mathrm{c}}(t), \hat{y}_{\mathrm{c}}(t), \frac{\dot{x}_{\mathrm{c}}(t)}{\dot{\xi}(t)}, \frac{\dot{y}_{\mathrm{c}}(t)}{\dot{\xi}(t)}, \hat{R}\right), \tag{B4}$$

where we have defined

$$\mathbf{d}_1 = \int_{-1}^{1} \mathbf{r}(\hat{x})\,\mathrm{d}\hat{x}, \tag{B5a}$$

$$\mathbf{d}_2\left(\hat{x}_{\mathrm{c}}(t), \hat{y}_{\mathrm{c}}(t), \frac{\dot{x}_{\mathrm{c}}(t)}{\dot{\xi}(t)}, \frac{\dot{y}_{\mathrm{c}}(t)}{\dot{\xi}(t)}, \hat{R}\right) = \int_{-1}^{1} \mathbf{r}(\hat{x}) f_1\left(\hat{x}_{\mathrm{c}}(t), \hat{y}_{\mathrm{c}}(t), \frac{\dot{x}_{\mathrm{c}}(t)}{\dot{\xi}(t)}, \frac{\dot{y}_{\mathrm{c}}(t)}{\dot{\xi}(t)}, \hat{R}(t), \hat{x}\right)\,\mathrm{d}\hat{x}, \tag{B5b}$$

$$\mathbf{K}_1 = \int_{-1}^{1} \mathbf{r}(\hat{x})\mathbf{b}_1^{\mathrm{T}}(\hat{x})\,\mathrm{d}\hat{x}, \tag{B5c}$$

$$\mathbf{K}_2\left(\hat{x}_{\mathrm{c}}(t), \hat{y}_{\mathrm{c}}(t), \hat{R}(t)\right) = \int_{-1}^{1} \mathbf{r}(\hat{x})\mathbf{b}_2^{\mathrm{T}}(\hat{x}_{\mathrm{c}}(t), \hat{y}_{\mathrm{c}}(t), \hat{R}(t), \hat{x})\,\mathrm{d}\hat{x}, \tag{B5d}$$

with

$$\mathbf{b}_1(\hat{x}) = \int_{-1}^{1} \frac{\mathbf{r}(\zeta)}{\pi}\frac{\sqrt{1-\zeta^2}}{(\hat{x}-\zeta)^2}\,\mathrm{d}\zeta, \tag{B6a}$$

$$\mathbf{b}_2(\hat{x}_{\mathrm{c}}, \hat{y}_{\mathrm{c}}, \hat{R}, \hat{x}) = \int_{-1}^{1} \mathbf{r}(\zeta)\sqrt{1-\zeta^2}\left.\frac{\partial g_{\mathrm{c}}(\hat{x}_{\mathrm{c}}, \hat{y}_{\mathrm{c}}, \hat{R}, \hat{x}, \hat{y}|\zeta, \eta)}{\partial\hat{y}\partial\eta}\right|_{\eta=0,\ \hat{y}=0}\,\mathrm{d}\zeta, \tag{B6b}$$

$$\begin{aligned} f_1\left(\hat{x}_{\mathrm{c}}, \hat{y}_{\mathrm{c}}, \frac{\dot{x}_{\mathrm{c}}}{\dot{\xi}}, \frac{\dot{y}_{\mathrm{c}}}{\dot{\xi}}, \hat{R}, \hat{x}\right) &= \int_{-\pi}^{\pi} \hat{R}\left(\frac{\dot{x}_{\mathrm{c}}}{\dot{\xi}}\cos\alpha + \frac{\dot{y}_{\mathrm{c}}}{\dot{\xi}}\sin\alpha\right) \\ &\times\left(\left.\frac{\partial g_{\mathrm{w}}(\hat{x}, \hat{y}|\hat{R}(t)\cos\alpha, \hat{R}(t)\sin\alpha)}{\partial\hat{y}}\right|_{\hat{y}=0} + \left.\frac{\partial g_{\mathrm{c}}(\hat{x}_{\mathrm{c}}, \hat{y}_{\mathrm{c}}, \hat{R}, \hat{x}, \hat{y}|\hat{R}(t)\cos\alpha, \hat{R}(t)\sin\alpha)}{\partial\hat{y}}\right|_{\hat{y}=0}\right)\,\mathrm{d}\alpha. \end{aligned} \tag{B6c}$$

The integral involving $\mathbf{b}_2$ is regular, thus, $\mathbf{K}_2$ can be numerically computed with ease. However, the integral for $\mathbf{b}_1$ is singular, thereby its principal value must be calculated. We compute the principal value analytically using Wolfram Mathematica software and then evaluate $\mathbf{K}_1$ numerically. The analytical expressions for $\mathbf{b}_1$ are presented until the eight power in ζ as

$$b_{1,1}(\hat{x}) = \int_{-1}^{1} \frac{\zeta^0}{\pi}\frac{\sqrt{1-\zeta^2}}{(\hat{x}-\zeta)^2}\,\mathrm{d}\zeta = -1, \tag{B7a}$$

$$b_{1,2}(\hat{x}) = \int_{-1}^{1} \frac{\zeta^1}{\pi}\frac{\sqrt{1-\zeta^2}}{(\hat{x}-\zeta)^2}\,\mathrm{d}\zeta = -2\hat{x}, \tag{B7b}$$

$$b_{1,3}(\hat{x}) = \int_{-1}^{1} \frac{\zeta^2}{\pi}\frac{\sqrt{1-\zeta^2}}{(\hat{x}-\zeta)^2}\,\mathrm{d}\zeta = \frac{1}{2}(1-6\hat{x}^2), \tag{B7c}$$

$$b_{1,4}(\hat{x}) = \int_{-1}^{1} \frac{\zeta^3}{\pi}\frac{\sqrt{1-\zeta^2}}{(\hat{x}-\zeta)^2}\,\mathrm{d}\zeta = \hat{x}(1-4\hat{x}^2), \tag{B7d}$$

$$b_{1,5}(\hat{x}) = \int_{-1}^{1} \frac{\zeta^4}{\pi} \frac{\sqrt{1-\zeta^2}}{(\hat{x}-\zeta)^2}\ \mathrm{d}\zeta = \frac{1}{8}(1+12\hat{x}^2-40\hat{x}^4), \tag{B7e}$$

$$b_{1,6}(\hat{x}) = \int_{-1}^{1} \frac{\zeta^5}{\pi} \frac{\sqrt{1-\zeta^2}}{(\hat{x}-\zeta)^2}\ \mathrm{d}\zeta = \frac{\hat{x}}{4}(1+8\hat{x}^2-24\hat{x}^4), \tag{B7f}$$

$$b_{1,7}(\hat{x}) = \int_{-1}^{1} \frac{\zeta^6}{\pi} \frac{\sqrt{1-\zeta^2}}{(\hat{x}-\zeta)^2}\ \mathrm{d}\zeta = \frac{1}{16}(1+6\hat{x}^2+40\hat{x}^4-112\hat{x}^6), \tag{B7g}$$

$$b_{1,8}(\hat{x}) = \int_{-1}^{1} \frac{\zeta^7}{\pi} \frac{\sqrt{1-\zeta^2}}{(\hat{x}-\zeta)^2}\ \mathrm{d}\zeta = \frac{\hat{x}}{8}(1+4\hat{x}^2+24\hat{x}^4-64\hat{x}^6). \tag{B7h}$$

Once $\mathbf{a}$ is computed at each time step from Eq. (B4), ϕ is known from Eq. (B2).

To close the semi-analytical solution, we need to compute ϕ_t and ϕ_x, and substitute them into Eqs. (1). The computation of ϕ_x is straighforward, therefore, it is omitted here. For ϕ_t, we have

$$\begin{aligned} \phi_t(\hat{x},0,t) &= a_1(t)\mathbf{r}^{\mathrm{T}}(\hat{x})\mathbf{Q}^{\mathrm{T}}\left(\dot{\mathbf{s}}_1(t)\dot{\xi}(t)+\mathbf{s}_1(t)\ddot{\xi}(t)\right)\sqrt{1-\hat{x}^2} \\ &+ \dot{a}_1(t)\dot{\xi}(t)\left(\mathbf{r}^{\mathrm{T}}(\hat{x})\sqrt{1-\hat{x}^2}-\hat{x}\mathbf{r}^{\mathrm{T}}_{\hat{x}}(\hat{x})\sqrt{1-\hat{x}^2}+\frac{\hat{x}^2\mathbf{r}^{\mathrm{T}}(\hat{x})}{\sqrt{1-\hat{x}^2}}\right)\mathbf{Q}^{\mathrm{T}}\mathbf{s}_1(t), \end{aligned} \tag{B8}$$

where the term including $\ddot{\xi}$ can be viewed as the added mass effect, while the rest as slamming force [7]. Here, $\dot{\mathbf{a}}$ is computed by differentiating Eq. (B4) with respect to t, such that

$$a_1(t)\mathbf{Q}\left(\mathbf{K}_1+\mathbf{K}_2(t)\right)\mathbf{Q}^{\mathrm{T}}\dot{\mathbf{s}}_1(t) = \mathbf{Q}\mathbf{K}_3(t)\mathbf{Q}^{\mathrm{T}}\mathbf{s}_1(t)-\mathbf{Q}\mathbf{d}_3(t), \tag{B9}$$

where

$$\begin{aligned} \mathbf{K}_3(t) = \int_{-1}^{1}\mathbf{r}(\hat{x})\Bigg(&\left((\hat{x}_{\mathrm{c}}(t)-a_2(t))\dot{a}_1(t)-\dot{a}_2(t)a_1(t)-\dot{x}_{\mathrm{c}}(t)\right)\frac{\partial\mathbf{b}_2^{\mathrm{T}}(\hat{x}_{\mathrm{c}}(t),\hat{y}_{\mathrm{c}}(t),\hat{R}(t),\hat{x})}{\partial\hat{x}_c} \\ &+\left(\hat{y}_{\mathrm{c}}(t)\dot{a}_1(t)-\dot{y}_{\mathrm{c}}(t)\right)\frac{\partial\mathbf{b}_2^{\mathrm{T}}(\hat{x}_{\mathrm{c}}(t),\hat{y}_{\mathrm{c}}(t),\hat{R}(t),\hat{x})}{\partial\hat{y}_{\mathrm{c}}}+\hat{R}\dot{a}_1(t)\frac{\partial\mathbf{b}_2^{\mathrm{T}}(\hat{x}_{\mathrm{c}}(t),\hat{y}_{\mathrm{c}}(t),\hat{R}(t),\hat{x})}{\partial\hat{R}}\Bigg)\ \mathrm{d}\hat{x}, \end{aligned} \tag{B10a}$$

$$\begin{aligned} \mathbf{d}_3(t) = \int_{-1}^{1}\mathbf{r}(\hat{x})\Bigg[&\left((\hat{x}_{\mathrm{c}}(t)-a_2(t))\dot{a}_1(t)-\dot{a}_2(t)a_1(t)-\dot{x}_{\mathrm{c}}(t)\right)\frac{\partial f_1\left(\hat{x}_{\mathrm{c}}(t),\hat{y}_{\mathrm{c}}(t),\frac{\dot{x}_{\mathrm{c}}(t)}{\dot{\xi}(t)},\frac{\dot{y}_{\mathrm{c}}(t)}{\dot{\xi}(t)},\hat{R}(t),\hat{x}\right)}{\partial\hat{x}_{\mathrm{c}}} \\ &+\left(\hat{y}_{\mathrm{c}}(t)\dot{a}_1(t)-\dot{y}_{\mathrm{c}}(t)\right)\frac{\partial f_1\left(\hat{x}_{\mathrm{c}}(t),\hat{y}_{\mathrm{c}}(t),\frac{\dot{x}_{\mathrm{c}}(t)}{\dot{\xi}(t)},\frac{\dot{y}_{\mathrm{c}}(t)}{\dot{\xi}(t)},\hat{R}(t),\hat{x}\right)}{\partial\hat{y}_{\mathrm{c}}}+\hat{R}(t)\dot{a}_1(t)\frac{\partial f_1\left(\hat{x}_{\mathrm{c}}(t),\hat{y}_{\mathrm{c}}(t),\frac{\dot{x}_{\mathrm{c}}(t)}{\dot{\xi}(t)},\frac{\dot{y}_{\mathrm{c}}(t)}{\dot{\xi}(t)},\hat{R}(t),\hat{x}\right)}{\partial\hat{R}} \\ &-a_1(t)f_2\left(\hat{x}_{\mathrm{c}}(t),\hat{y}_{\mathrm{c}}(t),\frac{\dot{x}_{\mathrm{c}}(t)}{\dot{\xi}^2(t)},\frac{\dot{y}_{\mathrm{c}}(t)}{\dot{\xi}^2(t)},\frac{\ddot{x}_{\mathrm{c}}(t)}{\dot{\xi}(t)},\frac{\ddot{y}_{\mathrm{c}}(t)}{\dot{\xi}(t)},\ddot{\xi}(t),\hat{R}(t),\hat{x}\right)\Bigg]\ \mathrm{d}\hat{x}, \end{aligned} \tag{B10b}$$

with

$$\begin{aligned} &f_2\left(\hat{x}_{\mathrm{c}},\hat{y}_{\mathrm{c}},\frac{\dot{x}_{\mathrm{c}}}{\dot{\xi}^2},\frac{\dot{y}_{\mathrm{c}}}{\dot{\xi}^2},\frac{\ddot{x}_{\mathrm{c}}}{\dot{\xi}},\frac{\ddot{y}_{\mathrm{c}}}{\dot{\xi}},\ddot{\xi},\hat{R},\hat{x}\right) = \\ &\int_{-\pi}^{\pi}\hat{R}\left(\left(\frac{\ddot{x}_{\mathrm{c}}}{\dot{\xi}}-\frac{\dot{x}_{\mathrm{c}}}{\dot{\xi}^2}\ddot{\xi}\right)\cos\alpha+\left(\frac{\ddot{y}_{\mathrm{c}}}{\dot{\xi}}-\frac{\dot{y}_{\mathrm{c}}}{\dot{\xi}^2}\ddot{\xi}\right)\sin\alpha\right)\frac{\partial g(\hat{x}_{\mathrm{c}},\hat{y}_{\mathrm{c}},\hat{R},\hat{x},\hat{y}|\hat{R}(t)\cos\alpha,\hat{R}(t)\sin\alpha)}{\partial\hat{y}}\Bigg|_{\hat{y}=0}\ \mathrm{d}\alpha. \end{aligned} \tag{B11}$$

Similarly, for ψ we can again posit

$$\psi(\hat{x},0,t) = \mathbf{P}^{\mathrm{T}}(\hat{x})\mathbf{s}_2(t)a_1(t)\xi(t)\sqrt{1-\hat{x}^2}, \tag{B12}$$

and substitute Eq. (B12) into Eq. (11) to establish

$$
\begin{aligned}
&\xi(t)\mathbf{Q}\left(\mathbf{K}_1+\mathbf{K}_2\left(\frac{x_\mathrm{c}(t)}{a_1(t)},\frac{y_\mathrm{c}(t)}{a_1(t)},\frac{R}{a_1(t)}\right)\right)\mathbf{Q}^\mathrm{T}\mathbf{s}_2(t)=\xi(t)\mathbf{Q}\mathbf{d}_1\\
&+\mathbf{Q}\mathbf{d}_2\left(\frac{x_\mathrm{c}(t)}{a_1(t)},\frac{y_\mathrm{c}(t)}{a_1(t)},l_x,l_y,\frac{R}{a_1(t)}\right)-a_1(t)\mathbf{Q}\mathbf{d}_4(a_2(t)),
\end{aligned}
\tag{B13}
$$

where

$$
\mathbf{d}_4(a_2(t))=\int_{-1}^{1}\mathbf{r}(\hat{x})|\hat{x}-a_2(t)|\tan\beta\ \mathrm{d}\hat{x}. \tag{B14}
$$

Substituting for ψ from Eq. (B12), we find that Eq. (12) is satisfied if and only if

$$
\mathbf{r}^\mathrm{T}(\pm1)\mathbf{Q}^\mathrm{T}\mathbf{s}_2(t)=0. \tag{B15}
$$

Eq. (B15) in combination with Eq. (B13) form a system of nonlinear algebraic equations that should be solved simultaneously to determine a_1 and a_2. Note that Eq. (B13) itself is a system of linear algebraic equations for $\mathbf{s}_2$, controlled by a_1 and a_2. We use the "mldivide" function in MATLAB to express $\mathbf{s}_2$ in Eq. (B15), based on the coefficient vectors and matrices of Eq. (B13). Then, the "fsolve" function in MATLAB is utilized to solve the nonlinear algebraic equations to determine a_1 and a_2.

The derivatives $\dot{a}_1$ and $\dot{a}_2$ can then be estimated by differentiating Eq. (B15) with respect to t, such that

$$
\mathbf{r}^\mathrm{T}(\pm1)\mathbf{Q}^\mathrm{T}\dot{\mathbf{s}}_2(t)=0, \tag{B16}
$$

where $\dot{\mathbf{s}}_2$ is substituted by differentiating Eq. (B13), that is,

$$
\begin{aligned}
&a_1(t)\xi(t)\mathbf{Q}\left(\mathbf{K}_1+\mathbf{K}_2\left(\hat{x}_\mathrm{c}(t),\hat{y}_\mathrm{c}(t),\hat{R}(t)\right)\right)\mathbf{Q}^\mathrm{T}\dot{\mathbf{s}}_2(t)=\\
&\mathbf{Q}\left(a_1(t)\dot{\xi}(t)\left(\mathbf{K}_1+\mathbf{K}_2\left(\hat{x}_\mathrm{c}(t),\hat{y}_\mathrm{c}(t),\hat{R}(t)\right)\right)+\dot{a}_1(t)\xi(t)\mathbf{K}_4(t)-\dot{a}_2(t)\xi(t)\mathbf{K}_5(t)-\xi(t)\mathbf{K}_6(t)\right)\mathbf{Q}^\mathrm{T}\mathbf{s}_2(t)\\
&-\dot{a}_1(t)\left(\mathbf{Q}\mathbf{d}_6(t)+a_1(t)\mathbf{Q}\mathbf{d}_4(a_2(t))\right)+\dot{a}_2(t)\left(-a_1(t)\mathbf{Q}\mathbf{d}_7(t)+a_1^2(t)\mathbf{Q}\mathbf{d}_8(t)\right)+\mathbf{Q}\mathbf{d}_5(t)+a_1(t)\dot{\xi}(t)\mathbf{Q}\mathbf{d}_1(t).
\end{aligned}
\tag{B17}
$$

Here,

$$
\begin{aligned}
\mathbf{d}_5(t)=\int_{-1}^{1}\mathbf{r}(\hat{x})\Bigg(&\dot{x}_c(t)\frac{\partial f_1\left(\hat{x}_\mathrm{c}(t),\hat{y}_\mathrm{c}(t),l_x(t),l_y(t),\hat{R}(t),\hat{x}\right)}{\partial\hat{x}_\mathrm{c}}\\
&\dot{y}_c(t)\frac{\partial f_1\left(\hat{x}_\mathrm{c}(t),\hat{y}_\mathrm{c}(t),l_x(t),l_y(t),\hat{R}(t),\hat{x}\right)}{\partial\hat{y}_\mathrm{c}}+a_1(t)f_2\left(\hat{x}_\mathrm{c}(t),\hat{y}_\mathrm{c}(t),\dot{x}_c,\dot{y}_c,\hat{R}(t),\hat{x}\right)\Bigg)\ \mathrm{d}\hat{x},
\end{aligned}
\tag{B18a}
$$

$$
\begin{aligned}
\mathbf{d}_6(t)=\int_{-1}^{1}\mathbf{r}(\hat{x})\Bigg[&(\hat{x}_\mathrm{c}(t)-a_2(t))\frac{\partial f_1\left(\hat{x}_\mathrm{c}(t),\hat{y}_\mathrm{c}(t),l_x(t),l_y(t),\hat{R}(t),\hat{x}\right)}{\partial\hat{x}_\mathrm{c}}\\
&+\hat{y}_\mathrm{c}(t)\frac{\partial f_1\left(\hat{x}_\mathrm{c}(t),\hat{y}_\mathrm{c}(t),l_x(t),l_y(t),\hat{R}(t),\hat{x}\right)}{\partial\hat{y}_\mathrm{c}}+\hat{R}(t)\frac{\partial f_1\left(\hat{x}_\mathrm{c}(t),\hat{y}_\mathrm{c}(t),l_x(t),l_y(t),\hat{R}(t),\hat{x}\right)}{\partial\hat{R}}\Bigg]\ \mathrm{d}\hat{x},
\end{aligned}
\tag{B18b}
$$

$$
\mathbf{d}_7(t)=\int_{-1}^{1}\mathbf{r}(\hat{x})\frac{f_1\left(\hat{x}_\mathrm{c}(t),\hat{y}_\mathrm{c}(t),l_x(t),l_y(t),\hat{R}(t),\hat{x}\right)}{\partial\hat{x}_\mathrm{c}}\ \mathrm{d}\hat{x}, \tag{B18c}
$$

$$
\mathbf{d}_8(t)=\int_{-1}^{1}\mathbf{r}(\hat{x})\ \mathrm{sign}\left(\hat{x}-a_2(t)\right)\tan\beta\ \mathrm{d}\hat{x}, \tag{B18d}
$$

$$\mathbf{K}_4(t) = \int_{-1}^{1} \mathbf{r}(\hat{x}) \Bigg((\hat{x}_\mathrm{c}(t) - a_2(t)) \frac{\partial \mathbf{b}_2^\mathrm{T}(\hat{x}_\mathrm{c}(t), \hat{y}_\mathrm{c}(t), \hat{R}(t), \hat{x})}{\partial \hat{x}_c} + \hat{y}_\mathrm{c}(t) \frac{\partial \mathbf{b}_2^\mathrm{T}(\hat{x}_\mathrm{c}(t), \hat{y}_\mathrm{c}(t), \hat{R}(t), \hat{x})}{\partial \hat{y}_c} \tag{B18e}$$

$$+ \hat{R}(t) \frac{\partial \mathbf{b}_2^\mathrm{T}(\hat{x}_\mathrm{c}(t), \hat{y}_\mathrm{c}(t), \hat{R}(t), \hat{x})}{\partial \hat{R}} \Bigg) \, \mathrm{d}\hat{x},$$

$$\mathbf{K}_5(t) = \int_{-1}^{1} a_1(t) \mathbf{r}(\hat{x}) \frac{\partial \mathbf{b}_2^\mathrm{T}(\hat{x}_\mathrm{c}(t), \hat{y}_\mathrm{c}(t), \hat{R}(t), \hat{x})}{\partial \hat{x}_c} \, \mathrm{d}\hat{x}, \tag{B18f}$$

$$\mathbf{K}_6(t) = \int_{-1}^{1} \mathbf{r}(\hat{x}) \left(\dot{x}_\mathrm{c}(t) \frac{\partial \mathbf{b}_2^\mathrm{T}(\hat{x}_\mathrm{c}(t), \hat{y}_\mathrm{c}(t), \hat{R}(t), \hat{x})}{\partial \hat{x}_c} + \dot{y}_\mathrm{c}(t) \frac{\partial \mathbf{b}_2^\mathrm{T}(\hat{x}_\mathrm{c}(t), \hat{y}_\mathrm{c}(t), \hat{R}(t), \hat{x})}{\partial \hat{y}_c} \right) \mathrm{d}\hat{x}, \tag{B18g}$$

where "sign($\cdot$)" represents the sign function. Eq. (B16) in combination with Eq. (B17) define a system of bilinear algebraic equations for unknowns $\dot{a}_1$ and $\dot{a}_2$. The procedure to compute $\dot{a}_1$ and $\dot{a}_2$ is similar to the one described for a_1 and a_2, and is therefore omitted for brevity. The only difference is that the "mldivide" function in MATLAB is used instead of "fsolve", since the system is linear.

[1] O. M. Faltinsen, *Sea Loads on Ships and Offshore Structures* (Cambridge University Press, New York, NY, 1990).

[2] S. Abrate, "Hull slamming," Applied Mechanics Reviews **64**, 060803 (2011).

[3] Y. M. Scolan and A. A. Korobkin, "Energy distribution from vertical impact of a three-dimensional solid body onto the flat free surface of an ideal fluid," Journal of Fluids and Structures **17**, 275–286 (2003).

[4] A. L. Facci and S. Ubertini, "Numerical assessment of similitude parameters and dimensional analysis for water entry problems," Mathematical Problems in Engineering **2015** (2015).

[5] E. F. Campana, A. Carcaterra, E. Ciappi, and A. Iafrati, "Some insights into slamming forces: compressible and incompressible phases," Proceedings of the Institution of Mechanical Engineers, Part C: Journal of Mechanical Engineering Science **214**, 881–888 (2000).

[6] D. Vella and Paul D. Metcalfe, "Surface tension dominated impact," Physics of Fluids **19**, 072108 (2007).

[7] O. M. Faltinsen, *Hydrodynamics of High-Speed Marine Vehicles* (Cambridge University Press, New York, NY, 2006).

[8] T. von Karman, "The impact on seaplane floats, during landing," NACA-TN-321 (1929).

[9] H. Wagner, "Uber stoss-und gleitvorgange an der ober- flache von flussigkeite," ZAMM-Zeitschrift fur Ange-wandte Mathematik und Mechanik **12**, 193–215 (1932).

[10] C. M. Seddon and M. Moatamedi, "Review of water entry with applications to aerospace structures," International Journal of Impact Engineering **32**, 1045–1067 (2006).

[11] B. Chang, M. Croson, L. Straker, S. Gart, C. Dove, J. Gerwin, and S. Jung, "How seabirds plunge-dive without injuries," Proceedings of the National Academy of Sciences , 201608628 (2016).

[12] J. W. Glasheen and T. A. McMahon, "A hydrodynamic model of locomotion in the basilisk lizard," Nature **380**, 340–342 (1996).

[13] A. Nila, S. Vanlanduit, S. Vepa, and W. Van Paepegem, "A PIV-based method for estimating slamming loads during water entry of rigid bodies," Measurement Science and Technology **24**, 045303 (2013).

[14] I. Stenius, A. Rosén, M. Battley, and T. Allen, "Experimental hydroelastic characterization of slamming loaded marine panels," Ocean Engineering **74**, 1–15 (2013).

[15] M. Porfiri and A. Shams, "Pressure reconstruction during water impact through particle image velocimetry: Methodology overview and applications to lightweight structures," Dynamic Response and Failure of Composite Materials and Structures (Edited by V. Lopresto, Al. Langella, and S. Abrate), Woodhead Publishing (2017).

[16] S. Wang and C. G. Soares, "Review of ship slamming," Journal of Marine Science and Application , 1–19 (2017).

[17] A. A. Korobkin, E. I Părău, and J. M. Vanden-Broeck, "The mathematical challenges and modelling of hydroelasticity," Philosophical Transactions of the Royal Society of London A: Mathematical, Physical and Engineering Sciences **369**, 2803–2812 (2011).

[18] R. Panciroli and M. Porfiri, "Analysis of hydroelastic slamming through particle image velocimetry," Journal of Sound and Vibration **347**, 63–78 (2015).

[19] X. Mei, Y. Liu, and D. K. Yue, "On the water impact of general two-dimensional sections," Applied Ocean Research **21**, 1–15 (1999).

[20] R. Panciroli, A. Shams, and M. Porfiri, "Experiments on the water entry of curved wedges: High speed imaging and particle image velocimetry," Ocean Engineering **94**, 213–222 (2015).

[21] S. Basak and A. Raman, "Hydrodynamic coupling between micromechanical beams oscillating in viscous fluids," Physics of Fluids **19**, 017105 (2007).

[22] M. Kimber, R. Lonergan, and S. V. Garimella, "Experimental study of aerodynamic damping in arrays of vibrating cantilevers," Journal of Fluids and Structures **25**, 1334–1347 (2009).

[23] S. Gupta, J. M. LeBlanc, and A. Shukla, "Sympathetic underwater implosion in a confining environment," Extreme

Mechanics Letters **3**, 123–129 (2015).
[24] M. S. U. Khalid, I. Akhtar, and H. Dong, "Hydrodynamics of a tandem fish school with asynchronous undulation of individuals," Journal of Fluids and Structures **66**, 19–35 (2016).
[25] M. Jalalisendi, A. Shams, R. Panciroli, and M. Porfiri, "Experimental reconstruction of three-dimensional hydrodynamic loading in water entry problems through particle image velocimetry," Experiments in Fluids **56**, 1–17 (2015).
[26] G. V. Logvinovich, "Hydrodynamics of flows with free boundaries," Naukova Dumka **128** (1969).
[27] A. A. Korobkin, "Analytical models of water impact," European Journal of Applied Mathematics **15**, 821–838 (2004).
[28] S. Russo, M. Jalalisendi, G. Falcucci, and M. Porfiri, "Experimental characterization of oblique and asymmetric water entry," Experimental Thermal and Fluid Science **92**, 141–161 (2018).
[29] W. Thielicke and E. J. Stamhuis, "PIVlab - Towards user-friendly, affordable and accurate digital particle image velocimetry in MATLAB," Journal of Open Research Software **2**, e30 (2014).
[30] Pressure measurements should be considered valid only after the sensor touches the water surface. The initial difference in the pressure readings is likely due to the combination of measurement uncertainty and variations in the installation process. Similar results were in fact noted in [28], without the presence of a cylinder.
[31] A. A. Korobkin, "Shallow-water impact problems," Journal of Engineering Mathematics **35**, 233–250 (1999).
[32] M. Jalalisendi, S. Zhao, and M. Porfiri, "Shallow water entry: modeling and experiment," Journal of Engineering Mathematics **104**, 131–156 (2017).
[33] C. P. Green and J. E. Sader, "Small amplitude oscillations of a thin beam immersed in a viscous fluid near a solid surface," Physics of Fluids **17**, 1–12 (2005).
[34] E. Grimaldi, M. Porfiri, and L. Soria, "Finite amplitude vibrations of a sharp-edged beam immersed in a viscous fluid near a solid surface," Journal of Applied Physics **112**, 104907 (2012).
[35] D. G Duffy, *Green's Functions with Applications* (Chapman & Hall/CRC Press, 2015).
[36] D. G. Duffy, *Mixed boundary value problems* (Chapman & Hall/CRC Press, 2008).
[37] A. A. Korobkin, "Advances in marine hydrodynamics," (Computational Mechanics, Boston, UK, 1996) Chap. Water impact problems in ship hydrodynamics, p. 323371.
[38] T. Gazzola, A. A. Korobkin, S. Malenica, and Y. M. Scolan, "Three-dimensional Wagner problem using variational inequalities," in *Proceedings of the International 20th Workshop on Water Waves and Floating Bodies, Longyearbyen, Norway, May* (2005).
[39] A. A. Korobkin, "Formulation of penetration problem as a variational inequality," Din. Sploshnoi Sredy **58**, 73–79 (1982).
[40] A. Shams, M. Jalalisendi, and M. Porfiri, "Experiments on the water entry of asymmetric wedges using particle image velocimetry," Physics of Fluids **27**, 027103 (2015).
[41] H. Jeffreys and B. Jeffreys, *Methods of Mathematical Physics* (Cambridge University Press, 1999).
[42] M. A. Cohen and Can O. Tan, "A polynomial approximation for arbitrary functions," Applied Mathematics Letters **25**, 1947–1952 (2012).